Journal of Hydrology 589 (2020) 125340

Contents lists available at ScienceDirect

Journal of Hydrology

journal homepage: www.elsevier.com/locate/jhydrol

Research papers

Monitoring of internal erosion processes by time-lapse electrical resistivity tomography

Matteo Masi[a,*], Farzad Ferdos[b], Gabriella Losito[c], Luca Solari[d]

[a] Department of Energy, Systems, Territory, and Construction Engineering, University of Pisa, Pisa, Italy
[b] Department of Civil and Architectural Engineering, Royal Institute of Technology (KTH), Stockholm, Sweden
[c] Department of Civil and Environmental Engineering, University of Florence, Florence, Italy
[d] Department of Civil and Environmental Engineering, University of Florence, Florence, Italy

ARTICLE INFO

This manuscript was handled by Corrado Corradini, Editor-in-Chief, with the assistance of Zhang Wen, Associate Editor

Keywords:
ERT
Resistivity imaging
Archie's law
Embankment dams
Internal erosion
Suffusion

ABSTRACT

Internal erosion phenomena are a major threat to all earthen structures, such as river levees and dams. Studying these phenomena has been limited because they occur concealed inside the material, which makes them difficult to observe and monitor. Non-destructive geophysical monitoring techniques are powerful tools that can provide insight into the processes involved. For this reason, a test rig has been specifically designed to conduct three-dimensional electrical resistivity tomography of soil specimens undergoing internal erosion due to seepage. Two suffusion tests were conducted where the erosion evolution has been monitored. The time-series of eroded mass weight were then used to correlate the changes in three-dimensional resistivity distribution to the porosity change in media by means of Archie's law. The results from the first suffusion test were used to calibrate Archie's model parameters. It was found that the resistivity variations were able to predict changes in the porous matrix structure. The data obtained from the second test were used to validate the model parameters and confirmed that the time-lapse three-dimensional inverted resistivity images were able to successfully quantify the global erosion rate.

1. Introduction

Internal erosion in earthen structures occurs when soil particles within the porous medium are transported by seeping water (Bonelli and Nicot, 2013). It represents a serious threat to the structural stability of embankment dams because the erosion process takes place deep inside the structure or its foundation (Wan and Fell, 2008). The hidden nature of internal erosion makes it both hard to detect as well as limiting the possibility of its investigation. Here the main problem is the common use of destructive methods to sample the affected soil regions both under field and laboratory conditions. There is a pressing need for detection methodologies that can preserve the soil sample in laboratory or in field cases (Fell et al., 2003). Geophysical methods are proven to be effective for identifying potential zones for internal erosion without causing any destruction in material. The most common methods are: ground-penetrating radar (GPR), Self-potential (SP), electrical resistivity tomography (ERT), electromagnetic (EM) methods, active and passive seismic methods as well as LIDAR and other remote sensing techniques. Among these only electrical (ERT, SP) and electromagnetic (EM, GPR) methods are directly sensitive to the presence of water in the embankment structure (Ikard et al., 2012; Panthulu et al., 2001).

GPR methods have the advantage of providing good resolution of the internal structures and are widely used for mapping lithological and sedimentological characterisation of quaternary deposit properties (Bakker and Van Der Meer, 2003; Carlsten et al., 1995; Smith and Jol, 1992; Trafford, 2009). The GPR's signals however, get severely attenuated when layers of fine grained soil are present. The latter is a prevailing property of earthen structures, specifically when the erosion susceptible zones are considered. However, SP and ERT methods are found to be more appropriate for structures that contain fine grained soils (Hirsch et al., 2008). SP and ERT are widely used to locate leakage prone and susceptible zones of embankment dams (Al-Fares, 2014, 2011; Bolève et al., 2011; Dahlin and Johansson, 1995; Ikard et al., 2015; Panthulu et al., 2001; Rittgers et al., 2014; Shin et al., 2019; Sjödahl et al., 2008; Soueid Ahmed et al., 2020; Titov et al., 2000). The ERT-based techniques have numerous advantages. They are cost-effective and easy to implement in the field; they can cover large earth volumes and the measurement can be performed repeated over time (time-lapse) and they do not require to be supervised (i.e. can be remotely operated). Moreover, they are highly sensitive to electrical

* Corresponding author.
E-mail addresses: m.masi@ing.unipi.it (M. Masi), ferdos@kth.se (F. Ferdos), losito@dicea.unifi.it (G. Losito), luca.solari@unifi.it (L. Solari).

https://doi.org/10.1016/j.jhydrol.2020.125340
Received 7 May 2020; Received in revised form 9 July 2020; Accepted 22 July 2020
Available online 28 July 2020

conductivity contrasts commonly found in the materials used for embankments construction. On the other hand, the fact that the method is subjected to site-specific conditions, and that the success of the study necessarily requires the integration of adequately large data collected for the specific case, are considered to be among the main disadvantages.

Dahlin et al. (2001) conducted resistivity and SP studies based on the surveying and monitoring data at the Sädva embankment in Sweden with the aim of to providing baseline information for evaluation of the SP monitoring data. The anomalies found in the collected SP data were correlated to known features of the dam construction while the other investigated areas presented smooth results with no major anomalies. Panthulu et al. (2001) used the same method to delineate seepage favourable zones for two of the Saddle dams of the Som-Kamla-Amba in India. A combination of SP method with salt tracer injections was used by Bolève et al. (2011) for localising seepage prone zones and quantifying the leakages in dams. There are also a number of studies that use the method to investigate seepage beneath homogeneous dams, e.g., a number of earth dams in Colorado (Ikard et al., 2015) and an embankment dam in California (Moore et al., 2011).

ERT methods are widely tested in dam monitoring. Johansson and Dahlin (1996) aimed to quantify the seepage and detect anomalous infiltration flow through monitoring seasonal resistivity variations in various case studies in Lövon and Moforsen embankment dam in Sweden. Similar case studies have been conducted by Al-Fares (2014, 2011) for characterizing the water leakage in Afamia-B and Abu Baara embankment dams in Syria. Sjödahl et al. (2010, 2008, 2005) performed extensive electrical resistivity investigation and monitoring for detection of internal erosion and anomalous seepage for four embankment dams in Scandinavia. In all of these studies, the measured data from the crest of the dams are inverted to a subsurface geoelectric section by various 2D inversion schemes (Constable et al., 1987; Loke and Barker, 1995) and the anomalous low resistivity zones in these 2D sections were interpreted as leakage zones.

Despite the effectiveness of SP and ERT methods, the 2D interpretation and quantification of the data are substantially affected by the 3D nature of the acquisition data. To overcome this limitation one option is to use cross-hole resistivity tomography by imaging the region between two boreholes in depth. Cross-hole data acquisition is done in depth in addition to the dam crest readings to provide the additional data. The application of this method are presented in numerous studies (e.g., Cho and Yeom, 2007; Daily and Owen, 1991; Lesur et al., 1999a,b; Park and Van, 1991; Shima, 1992). Fargier et al. (2014) suggest an alternative method for monitoring an embankment dike with the conventional data acquisition procedure with linear arrays. They developed a new extended normalisation technique, by providing, during inversion, a set of pre-processed apparent resistivities that are not affected by external 3D effects. In this way, the artifacts of conventional 2D inversion due to the 3D nature of embankment dike are reduced.

3D surveys can also be conducted by using a rectangular grid of electrodes instead of linear array at the surface. This method has been reported to provide a good resolution (Chambers et al., 2002, 2011; Dahlin et al., 2002; Gharibi and Bentley, 2005). However, irrespective of the method to get a workable resolution, a larger number of electrodes are needed in the survey grid, as well as the need for a larger number of acquisition combination. For this reason, some 3D array optimization algorithm must be applied to minimize the number of acquisitions of data registering at multiple electrodes with multichannel instrumentation and filtering out potentially unstable arrays (Loke et al., 2014). Here, stable and robust time-lapse inversion techniques, which can be incorporated into automatic inversion software, should be used to produce interpretable images.

The foregoing survey suggests that ERT method has the potential to monitor the internal erosion processes and their development in a controlled laboratory environment. It can provide insight into the internal erosion processes involved and thereby improving our understanding of the factors that affect the resistivity response when internal erosion phenomena are triggered. The main aim of the present work is to investigate these processes by time-lapse three-dimensional electrical resistivity tomography. For this purpose, a high-resolution resistivity probe system was designed and integrated into an apparatus for studying phenomenon of internal erosion (e.g. suffusion phenomenon) at laboratory scale. 3D electrical resistivity profiles of soil material were produced, so that changes in porous matrix could be visualised and quantified.

2. Materials and methods

2.1. Forward modelling

Using electrical resistivity tomography, the distribution of the electrical properties inside the medium can be determined from a set of measurements taken on the boundary. It involves defining a forward model in which the response is calculated by assigning electrical properties to the model elements.

The governing equation for the ERT forward model is the Poisson's equation:

$$\nabla \cdot \mathbf{J} = Q_j \tag{1}$$

in which $\mathbf{J}$ (A m^{-2}) denotes the electric current density and Q_j (A m^{-3}) is the boundary current source. Under electrostatic conditions, the electric potential V (V) can be written as $\mathbf{E} = -\nabla V$, where $\mathbf{E}$ (V m^{-1}) is the electric field. The flow of current is given by the Ohm's law:

$$\mathbf{J} = \sigma \mathbf{E} \tag{2}$$

in which σ (S m^{-1}) is the electric conductivity.

Combining Eqs. (1) and (2) the ERT forward problem can be described by:

$$-\nabla \cdot (\sigma \Delta V) = Q_j \tag{3}$$

The physical boundaries of the experimental rig consisted of insulating walls, therefore Neumann boundary conditions were applied at these surfaces. The numerical methods used to solve the forward model will be described in the next sections (paragraphs 2.7 and 2.8).

2.2. Inverse modelling

The inverse problem involves the determination of the specific parameter distribution (i.e. resistivity) that minimizes the discrepancy between measured and calculated values (i.e. the inverse model is used for the calibration of the forward model). The approach of inverse problem solving is a process of calculating from a set of data the causal factors that produced them which in turn is characterized by some degree of non-uniqueness for the solution. Consequently, formulation of the inverse model usually requires mathematical regularization of the model parameters by introducing additional constraints to reduce the degrees of freedom and achieve convergence of a unique solution (Binley, 2015). The inverse problem is formulated as an optimization problem, involving the minimization of the objective function S defined as:

$$S = \Phi_d + \alpha \Phi_m \tag{4}$$

in which Φ_d represents the Chi-squared measure of data misfit, Φ_m is the model objective function containing the selected regularization scheme and α is the regularization parameter, used to control the weight of the regularization with respect to the data misfit.

For N measured data d_i, with associated standard deviation of ε_i, the Chi-squared measure of the data misfit is defined as:

$$\Phi_d = \sum_{i=1}^{N} \left(\frac{d_i - f_i(\mathbf{m})}{\varepsilon_i} \right)^2 \tag{5}$$

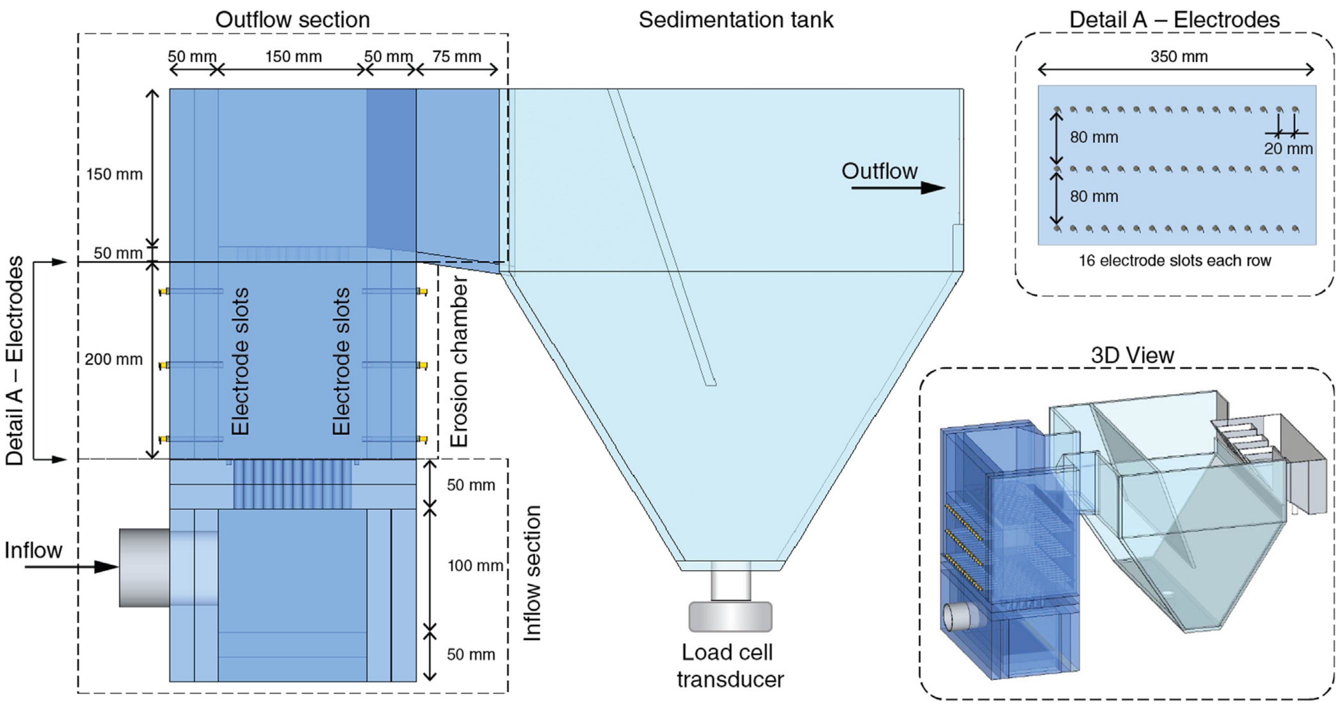

Fig. 1. Experimental apparatus for internal erosion tests, adapted from Ferdos et al. (2018).

in which f_i denotes the forward model operator and $\boldsymbol{m}$ the vector of parameters.

For inversion, the following scheme (referred to as Occam's inversion) involving minimization of the objective function S is considered:

$$S = \|\mathbf{W_d}(\mathbf{d} - \mathbf{f}(\mathbf{m}))\|^2 + \alpha\|\mathbf{W_m}\,\mathbf{m}\,\|^2 \tag{6}$$

in which $\boldsymbol{W_d}$ is the data weighting matrix, assumed to be diagonal with diagonal values $W_{i,i} = 1/\varepsilon_i$ and $\boldsymbol{W_m}$ is a first-order spatial smoothing operator (see Kemna, 2000).

The numerical implementation of the minimization of the objective function (Eq. (6)) can be achieved by using an iterative process, i.e. Gauss-Newton algorithm which yields the following iterative equation (Binley and Kemna, 2005):

$$(\mathbf{J^T W_d^T W_d J} + \alpha\mathbf{R})\Delta\mathbf{m} = \mathbf{J^T W_d^T}(\mathbf{d} - \mathbf{f}(\mathbf{m_k})) - \alpha\mathbf{R m} \tag{7}$$

in which $\mathbf{J}$ is the Jacobian such that $J_{i,j} = \partial d_i/\partial m_j$, $\mathbf{R}$ is the roughness matrix which describes the connectivity of the parameters and $\Delta\mathbf{m}$ the model update at each iteration. Starting from a model $\mathbf{m_0}$, the iteration process $\mathbf{m_{k+1}} = \mathbf{m_k} + \Delta\mathbf{m}$ is carried out. An additional algorithm is employed to make an optimal choice of the regularisation parameter α at each iteration (deGroot-Hedlin and Constable, 1990).

2.3. Porosity-resistivity relationship

To relate the electrical properties of the soil to its porous matrix structure, some constitutive law needs to be introduced. The Archie's law (Archie, 1942) is the most common law for relating resistivity to porosity. This empirical law was first introduced to quantify the relationship between porosity, electrical conductivity and brine saturation of hydrocarbon-bearing porous sedimentary rocks. It laid the foundation for interpretation of electrical conductivity of a media to its porous structure. The original form of the Archie's law is valid for medium to coarse-grained soils and cobbles. When clay particles are present, the assumption that the soil matrix is an electrical insulator may no longer be valid. In this case, an additional electrical conduction path, namely the surface conductivity exists, which originates from the electrical double layer forming around charged clay minerals. To include this aspect, a petrophysical relationship, which includes an additional term for the surface conductivity was proposed by Waxman and Smits (1968) and later applied in several more recent studies (Breede et al., 2011; Schmutz et al., 2010):

$$\sigma = \frac{S_w^n}{F}\left(\sigma_w + \frac{\sigma_s}{S_w}\right) \tag{8}$$

in which, σ is the bulk conductivity of the porous material (S m^{-1}), σ_w is the pore water conductivity (S m^{-1}), σ_s is the surface conductivity (S m^{-1}), S_w is the water saturation (–), n is the saturation exponent (–) and F is the formation factor. The formation factor is defined as $F = a\phi^{-m}$ where ϕ is the porosity of the medium, m is the cementation exponent, and a is 1 in the original Archie's formulation; in some cases, the additional parameter a is $\neq 1$ for a better fit (Schön, 2015). Exponent m is a porous matrix dependent constant which is related to the grains size and shape in the medium, porous structure and its network length and distribution. For a pore network of parallel capillary tubes, m could be assigned 1. For unconsolidated sands, m, observed is about 1.3 and for porous sedimentary rocks it varies in the range 1.7–4.1 (Archie, 1942). Instead, as pointed out by Glover (2016), the value assumed by a should be as close to 1 as possible, since the introduction of this parameter in the Archie's law has no actual physical meaning. However, since in most measurements systematic errors can be present, a non-unity value of the parameter a is justified to compensate for those errors which may be present in both electrical and porosity data.

2.4. Experimental apparatus for erosion tests

The experimental set-up, described in Ferdos et al. (2018), consisted of an erosion rig, a water supply system, a set of measurement instruments for process monitoring and an ERT measurement system. A schematic illustration of the experimental apparatus is given in Fig. 1. The erosion rig assembly consisted of the following parts: an inflow section, an erosion chamber, an outflow section and a sedimentation tank. All the parts were made of Plexiglas and were externally framed by stainless steel for reinforcement.

The erosion chamber had inner dimensions of 350 × 200 × 150 mm. The porous medium test specimen was inserted inside the erosion chamber and it was confined by the rigid walls laterally. The specimen was vertically confined by means of perforated plates at the top and at the bottom of the specimen; the top plate was 15 mm in thickness with 96 holes each 20 mm holes and was pressed by a piston rod with a specified load. The plate at the bottom was 100 mm in thickness with 96 holes, each 10 mm in diameter. A plastic filter mesh was placed between the specimen and the perforated rigid bottom plate that only permitted water inflow.

Hydraulic loading of the test specimen was applied by means of water head control, using inlet and outlet tanks. A municipality water system was used to supply the inlet tank with clean water. An overflow on the inlet tank bypassed the excess flow, and hence maintained a constant water head at the bottom of the test specimen. Water flow rate was measured by using a magnetic flow meter appropriate for low flows. Water electrical conductivity and temperature were monitored manually at regular intervals of about 1 h.

Eroded material from the soil specimen was collected in the sedimentation tank located downstream the erosion rig. A load cell transducer was installed at the bottom of the sedimentation tank to monitor its weight, with a resolution of ± 0.01 g. This setup allowed for continuous monitoring of the mass of the particles eroded from the specimen during the tests.

The electrodes were placed in 6 rows spaced 80 mm, with 16 electrode slots each row, spaced 20 mm, allowing the installation of up to 96 electrodes. The electrode slots were 8 mm in diameter, while the electrodes were stainless steel rods with 5 mm diameter. In the present work, half of the slots were used, therefore a total of 48 electrodes, spaced 40 mm, were installed. The choice of the electrode material and positioning is further discussed below.

2.5. ERT measurement system

The ERT data acquisition was carried out with a custom-built tomography system, specifically designed for laboratory measurements with a multi-electrode configuration, with 48 channels. It worked efficiently, by the optimization of the acquisition scheme and multichannel measurements. The main parts of the system were a PC which controlled I/O cards (multiplexers) through a microcontroller, an external current generator, a digital acquisition device (DAQ), a power supply, and the electrodes. The whole system was designed based on the system previously developed at Central Institute for Electronics (ZEL), Forschungszentrum Julich, Germany (Zimmermann et al., 2008) and it is an upgraded version of the system described in Masi and Losito (2015), modified to implement the multi-channel capabilities. The block diagram is shown in Fig. 2.

Current injection was achieved by using a function generator (Agilent 33120A) and the type of signal injected was a sine wave (AC current). The current was measured by reading the voltage drop across a precision low-resistance shunt resistor of known value; the latter signal was amplified using a high-precision programmable gain amplifier (PGA) and then fed to one channel of the acquisition card. The acquisition card had 8 simultaneous analog inputs, with one analog-to-digital converter (ADC) per channel, with 16-bit resolution.

To perform data acquisition in 48-electrode mode, a multiplexer circuit was needed for switching the current injector and voltmeter among the different channels. The current injection multiplexer was capable of selecting two electrodes for injecting the current into the sample. The voltage multiplexer, instead, was capable of selecting 6 electrodes to measure the voltage response of the sample at up to 6 locations.

The electrodes were connected to external circuits which allowed the same electrode to be switched from acquisition to current injection mode by means of relays activated by the current injection multiplexers. In acquisition mode, the signals from the potential electrodes were fed to an amplifier circuit and then routed to the ADCs by the voltage multiplexer. The amplifier circuit consisted of a unit gain operational amplifier; its high-impedance (1 TΩ) prevented the polarization of potential electrodes and its low output impedance reduced the capacitive coupling effects within the instrumentation.

The whole system was controlled by specifically developed LabVIEW code, executed on a standard laptop computer. The software could generate the acquisition sequence for the scheduling the measurements, as well as generating the signals, controlling the multiplexers and the acquisition device, and post-processing the data.

2.6. Electrode material

The choices of electrode material and positioning are particularly critical for ERT measurements since the amplitude response can be affected by systematic errors due to the wrong choices of these two factors. The common materials employed as current/potential electrodes are stainless steel, iron, copper, silver, aluminum, brass, titanium with mixed metal oxide coating, carbon and metal-salt-compound (non-polarizable) electrodes. The response of these electrodes were investigated by many authors (De Donno and Cardarelli, 2011; Deceuster et al., 2013; LaBrecque and Daily, 2008; Vanhala and Soininen, 1995) in order to evaluate the error in the measurements as a consequence of the materials selected. Most of the authors agree that the best performing electrodes are the non-polarizable ones, but they could not be employed in the present work as they were not suitable for the operating conditions of internal erosion tests. They are usually built with a porous plug separating the measurement environment from the electrolyte in which the electrodes are immersed for protection. The water pressure would allow the water to enter inside the electrode body and thus damaging the electrodes.

The electrode material has to be stable over time and should not be affected by oxidation/corrosion or any other chemical/electrochemical effects. As reported by LaBrecque and Daily (2008), stainless steel and iron electrodes are observed to have a better response compared to the other investigated materials, both for resistivity and chargeability in the time domain.

The use of carbon/graphite electrodes was also considered for installation. Carbon electrodes are not subjected to redox reactions with the surrounding electrolyte (i.e. the soil water content in erosion tests) and they are durable and stable in long term monitoring applications. However, they have higher resistance that can lead to their polarization (ohmic polarization) when they are immersed in the current path of an electric field. Furthermore, the response of carbon electrode is subjected to relevant errors, especially for chargeability measurements (LaBrecque and Daily, 2008).

In the present study, we selected stainless steel electrodes with the aim of minimizing contact resistance with the electrolyte, being the most critical aspect within the scope of this work.

2.7. Electrode positioning

In ERT measurements electrode polarization is a substantial source of error. To minimize the polarization effect due to voltage gradients and ohmic losses through the electrode material, the position of the electrodes must to be carefully optimized with respect to the electric field by placing the electrodes outside the current path. To study the effect of electrode positioning, a forward 3D model was implemented in Python language, using the open-source FEniCS package (Alnæs et al., 2015). FEniCS allowed us to solve the ERT forward problem (Eq. (3)) with the finite element method and compute the electric potential and current density distributions. We used the open source software "gmsh" (Geuzaine and Remacle, 2009) to generate the 3D finite element mesh. The elements of the mesh had a tetrahedral shape.

The simulated domain consisted of a box having the dimensions of the erosion chamber (350 × 200 × 150 mm) and 4 cylindrical electrode slots (diameter 8 mm) spaced 40 mm. The box was filled with a homogeneous material having 200 Ωm resistivity, simulating the expected resistivity of the soil specimen used for erosion tests. Two

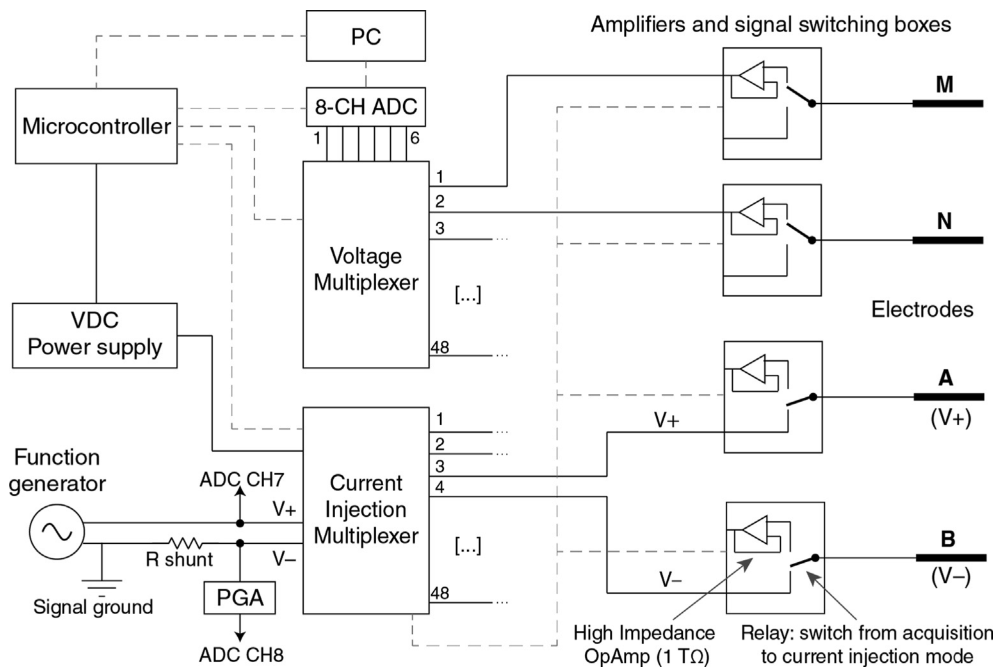

Fig. 2. Schematic diagram of the measurement setup. Solid lines represent analogue signal paths while dashed lines are digital buses.

electrodes (A and B) were used for current injection in the model and two for potential measurements. Electrode A was assigned a value of electric potential of 5 V, while electrode B served as the ground (0 V). Therefore, in the numerical simulations the boundary conditions at the electrodes were of Dirichlet type.

The electric potential and the current density distributions from the simulation are shown in Fig. 3. The figure shows the middle sections along the z-axis.

The distribution of the current density magnitude is shown in the Fig. 3b, which illustrates the field for the entire section and a detailed view of the M electrode on the right.

Fig. 4 shows the current density inside the cavity of the electrode slots along a cut line parallel to the y-axis placed at the midpoint of the cavity. The current density decreases with the distance from the inner border of the Plexiglas wall (corresponding to $y = 0$ in Fig. 3). It can be observed that the current density inside the M electrode slot is about 1.5×10^{-2} A/m^2 (-10 mm from the border) in the soil bulk and it decreases substantially inside the cavity. On the border of the cavity, the current density is 1.0×10^{-2} A/m^2 (0 mm from the border) in which decreases quickly and substantially and reaches the amount

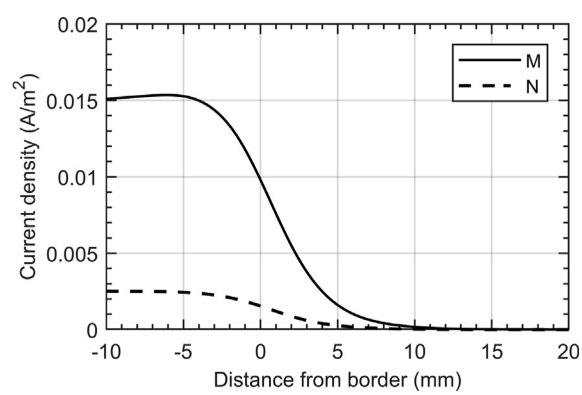

Fig. 4. Current density inside the electrode slots as a function of the distance from the Plexiglas border. The distance is referred to an outward-pointing normal, i.e., positive distance values refers to areas inside the electrode cavity while negative values to areas in the soil bulk.

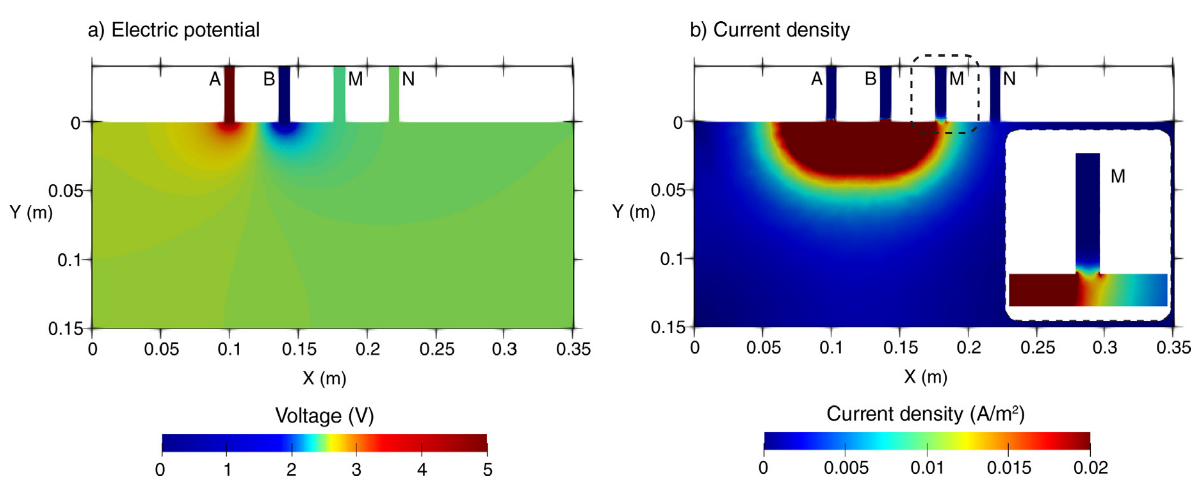

Fig. 3. Sections along the z-axis of the 3D simulations; a) electric potential and b) current density (magnitude) distribution.

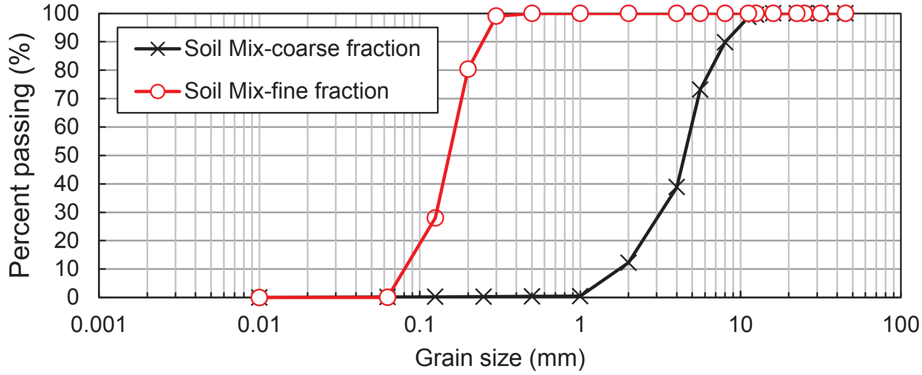

Fig. 5. Soil gradation of coarse and fine fractions of the soil mix for the erosion tests.

1.5×10^{-4} A/m^2 at 10 mm distance from the border and 1.5×10^{-8} A/m^2 at the bottom of the cavity (20 mm from the border).

The numerical simulations suggested that the electrodes must be installed inside the electrode cavity in order to place the electrode outside the current path. The tip of the electrode should be at least 5 mm inwards from the border to achieve an attenuation of the current density of about 1/10 with respect to the current density in the bulk. Therefore, the distance should be at least of the order of magnitude of the diameter of the opening for the electrode. Furthermore, when the electrode is placed 10 mm away from the border the attenuation is about 1/100, leading to very small polarization errors which have been adopted in the installation of the electrodes on the erosion chamber.

2.8. Experimental protocol

Experimental protocol involved the choices of material properties and experimental conditions. The soil used in erosion tests consisted of a mixture composed of gravel and sand with varying specific grain size ranges. Test specimens were prepared by mixing different size ranges to obtain the target gradation curve tested by Skempton and Brogan (1994), referred to as the "soil-A" gap graded sandy gravel soil. Soil mix grading is presented in Fig. 5. The rationale for performing tests on this specific gap graded and susceptible soil was that the soil fulfilled the granulometric criteria for the internal instability for suffusion erosion phenomena (see Ferdos et al., 2018).

The objectives of the suffusion tests were to evaluate the mass erosion rate and quantify the porosity variations of the specimens by means of time-lapse 3D tomography. Two tests were carried out under two different mechanical loading of equivalent to 0 and 10 kPa vertical stress application on the top of the specimen, respectively. Both tests were carried out under constant hydraulic loading, where the specimen was loaded until reaching the initiation of erosion. After the detection of initiation, the mechanical and the upstream water head were kept constant and the mass removal was monitored. Moreover, the hydraulic conductivity of the porous medium was estimated based on Darcy's law and monitored during the tests.

The suffusion process was monitored by conducting 3D resistivity measurements, taken at the start of each test, then after initiation at one-hour intervals until the end of the test. A continues monitoring of eroded sediments were also done which were used for calibration and validation studies of the 3D-ERT acquisitions.

The protocol for ERT measurements involved: the selection of the measurement sequence, the definition of the inverse model and its validation, and the estimation of data errors.

All the ERT measurements were carried out by injecting 20 cycles of a 150 Hz sine-wave. The measurement sequence consisted of dipole–-dipole arrays. The sequences were optimized in order to achieve both the best possible signal-to-noise ratio (SNR) and model resolution; for erosion tests they were further optimized to obtain a faster acquisition, because of the time-dependent behaviour of the erosion processes.

The 3D inversions were performed with the software package R3t (Binley, 2019), which solves the forward model by the finite element method and implements the iterative solution of Eq. (6), through Eq. (7). In the forward model, the boundary conditions at the electrodes were Neumann-type, to represent the injection of the current of known magnitude as performed during the measurements. To set up the 3D finite element mesh required as input to R3t, we used the gmsh software. The mesh consisted of tetrahedral elements and its geometry and characteristics were chosen to be as close as possible to the physical model, by individually separating the resistivity zones of the various parts of the experimental rig. These included (with reference to Fig. 1): the resistivity of the top perforated Plexiglas plate, the bottom Plexiglas plate, the water at the top of the soil in the outflow section, the water inside chamber at the inflow section, and the specimen in the erosion chamber. Only the resistivity of the specimen was made variable during the inversions, while the resistivity value of the other parts was kept fixed. A mesh sensitivity study was also performed in order to identify the required mesh size for the present problem.

The measurements had to be taken in the shortest time as possible, therefore it was not convenient to perform reciprocal measurements because they would have increased significantly the acquisition period. For this reason, we performed an error analysis based on the noise in the acquired signals. The errors in the data were considered to be proportional to the noise measured at the potential electrodes, due to the fact that the signal of the electric current was found to be significantly stronger at the range of impedances measured during the experiments and less susceptible to environmental noise than the signals of electric potential. Moreover, the channel for current signal acquisition had a dedicated PGA, as described above, which further helped to increase the signal-to-noise ratio (SNR) before the ADC conversion. Under this hypothesis, for each measurement the SNR of the differential signal between electrode M and N was calculated. The amplitude of the background noise was computed by summing the amplitude of all harmonic components of the signal excluding the fundamental frequency. The standard deviation of the measured resistance was thus considered to be proportional to the standard deviation of the background noise.

A summary of the ERT parameters and experimental conditions for the erosion tests is reported in Table 1.

3. Results and discussion

3.1. ERT inverse model validation

Model validation involved three steps: 1) optimal choice seeking of the boundaries, 2) numerical model mesh sensitivity tests, and 3) inverse model experimental validation.

Table 1
ERT model parameters and experimental conditions for internal erosion tests.

Parameters	Mesh sensitivity test	Setup validation test	Suffusion – exp. A	Suffusion – exp. B	Unit
ERT model parameters					
Mesh – number of cells	13,430/42,779	42,779	42,779	42,779	–
Mesh – min. element size	0.02/0.01	0.01	0.01	0.01	m
Number of dipoles	6390	5814	3763	3720	–
Number of time-lapse meas.	–	–	18	26	–
Time-lapse interval	–	–	1	1	hours
Top plate resistivity	not present	not present	100	100	Ωm
Bottom plate resistivity	600	600	600	600	Ωm
Water boundaries resistivity	24	4	23	23	Ωm
Initial model resistivity	24	4	250	250	Ωm
Erosion tests – experimental conditions					
Experiment duration	–	–	21	28	hours
Load	–	–	0	10	kPa
Applied water head (after erosion started)	–	–	170	270	mm
Flow rate (start)	–	–	1.3×10^{-5}	1.9×10^{-5}	$m^3 s^{-1}$
Flow rate (end)	–	–	4.2×10^{-5}	3.8×10^{-5}	$m^3 s^{-1}$
Hydraulic conductivity (start)	–	–	2.9×10^{-4}	2.7×10^{-4}	$m s^{-1}$
Hydraulic conductivity (end)	–	–	9.4×10^{-4}	5.4×10^{-4}	$m s^{-1}$

3.1.1. Selection of boundaries

The mesh used for the inversions is shown in Fig. 6. To accurately replicate the geometry of the erosion rig and its properties, different arrangements of the boundaries were tested. Both the top and bottom perforated Plexiglas plates were included in the model as well as the water at the bottom and at the top in the inlet and outlet sections respectively to include their influence on the measured data.

A fixed resistivity value was assigned to Plexiglas components because their values were constant during the experiments. For the water components a constant resistivity value was assigned since the resistivity of water changed slightly during the experiments (less than 8%). The water temperature was relatively stable during the experiments with a mean value of 14 °C and a maximum variation of ± 2 °C. Thus, assigning a constant resistivity value allowed for constraining the model and prevented the inversion procedure from trying to change their values during the inversions.

The value of the resistivity of the water was directly assigned from the measured data conducted during the tests for the two regions at the top and at the bottom of the 3D domain (values are reported in Table 1). The resistivity of the Plexiglas plates however was not determined directly. The difficulty was that the perforated Plexiglas plates do not have an isotropic resistivity i.e. the resistivity depends on the direction of the electric field. Thus, the apparent resistivity of the Plexiglas filter cannot be estimated merely on the basis of the filter geometry. Because of this difficulty in the calculation of the actual resistivity "observed" from the electrodes, the resistivity of these two Plexiglas filters were manually calibrated to get the minimum possible error (RMS misfit) between the inverse model and the observed data. With this procedure, a value of 100 Ωm was assigned to the plate at the top and 600 Ωm to the thicker plate at the bottom.

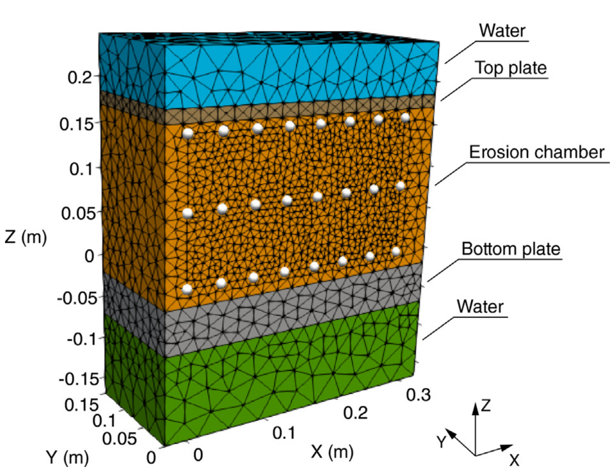

Fig. 6. Model mesh and boundaries.

3.1.2. Mesh sensitivity study

The results of the inversions must be evaluated with regard to the discrepancy of the optimized model from the measured data. It implies that the results could be influenced by the size of the parameter block size (discretisation). It is therefore necessary to select a mesh size that minimizes the error between the model and monitored data. However, the number of model parameters must also be limited to avoid any increase in uncertainty due to raising number of parameters to be optimized. Thus, a mesh sensitivity analysis is essential in order to choose the best performing mesh for the problem.

To examine the influence of the mesh size on the results of the inverse model, optimisation studies were carried out for the erosion chamber filled only with tap water whereby the resistivity parameter of the filling material as well as the expected inversion results were known. A correct inversion should display a homogeneous resistivity distribution since the filling material is tap water only.

We conducted two sets of measurements with different mesh sizes, by filling the chamber with water having a resistivity of 24 Ωm. The results of the inversions are shown in Fig. 7.

Fig. 7 shows that the distribution of the inverted resistivity is not fully homogeneous. The origin of this inhomogeneity is related to the measurement process, model setup and inversion errors. Considering the two meshes, the coarse mesh, with 20 mm mesh block size, gave an inverse model which showed a wider spread in the resistivity values in comparison with the finer mesh model. This can be seen from the histogram to the right of the resistivity contours. The finer mesh produced a resistivity distribution which is closer to the real and expected one for water, having less spread of the resistivity values. It was found that both increasing the number of elements and decreasing the mesh block sizes to less than 10 mm resulted in increased spreading the histogram of the resistivity values and further inhomogeneity in predicting the resistivity of the mesh elements. The conclusion was that a mesh size of 10 mm would be optimal size for discretization of the inverse model. The optimized mesh had a total of 42,779 elements.

3.1.3. Setup validation

After the model mesh and boundaries were set, a controlled experimental test was carried out to find the best acquisition system and to validate the inverse model. The erosion chamber was filled with tap water and tempered with adding some NaCl to reach a resistivity of

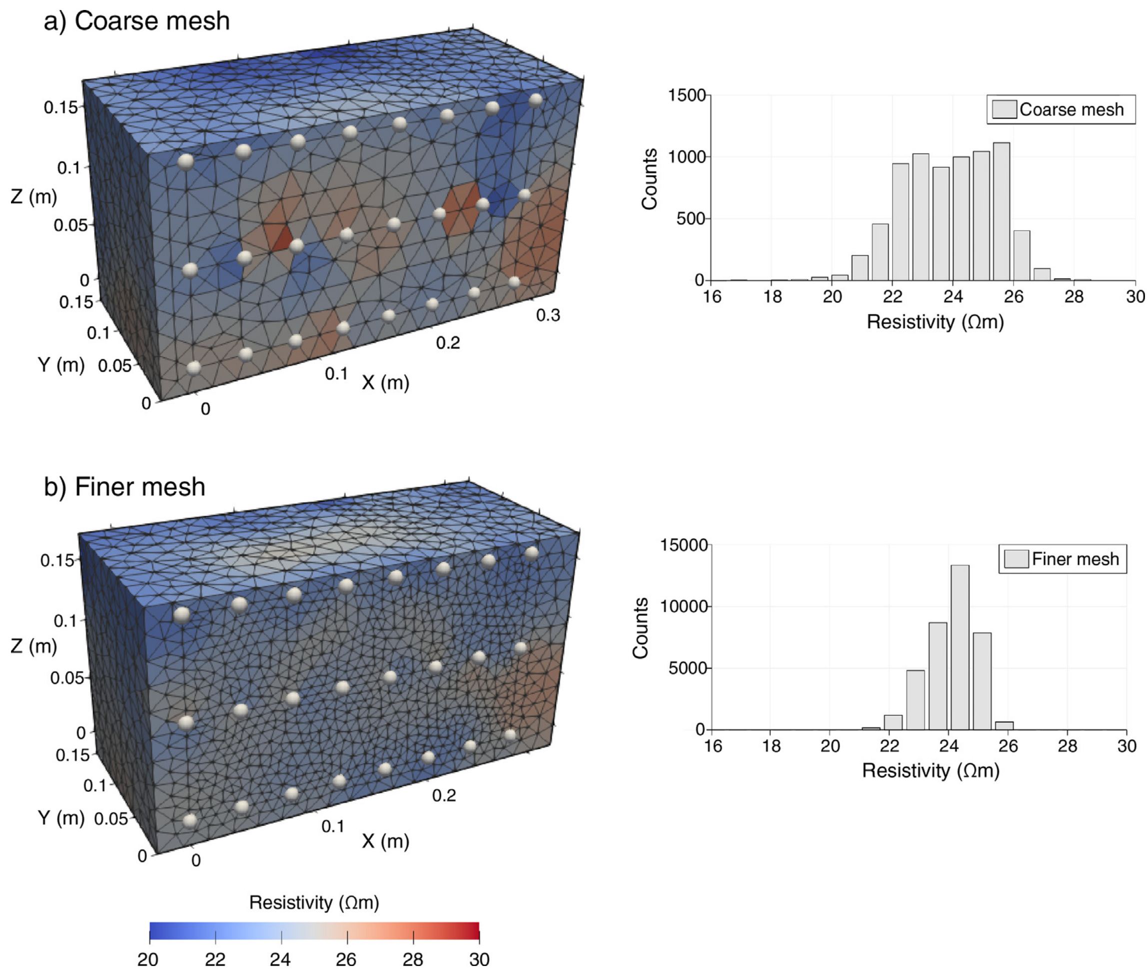

Fig. 7. Comparison of inversion of water-filled cell with coarse mesh (a) with mesh size 20 mm and finer mesh (b) with mesh size 10 mm with their histogram of the resistivity parameter value to the right.

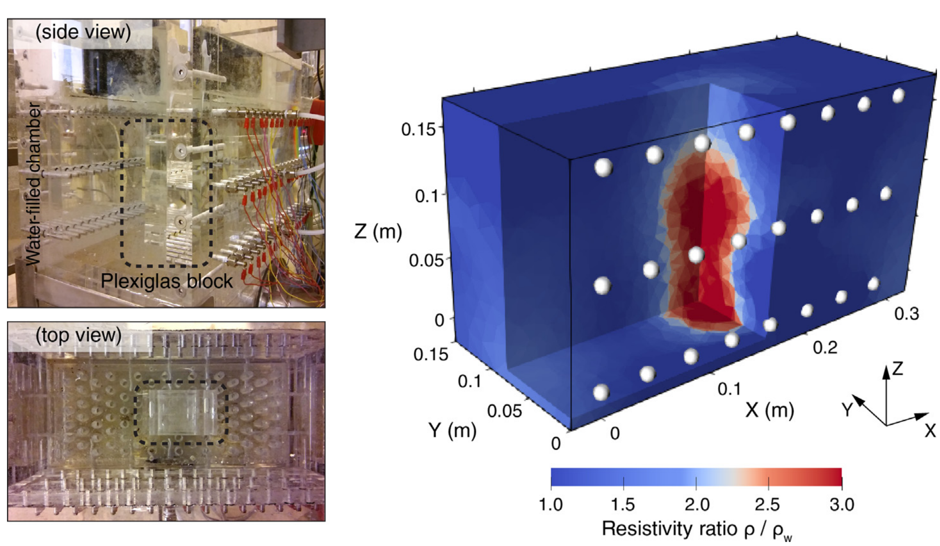

Fig. 8. Inversion test of water filled chamber with a Plexiglas block in the middle.

4 Ωm. A block of Plexiglas was placed in the middle of the chamber and ERT measurement was performed. The results obtained are shown in Fig. 8.

Fig. 8 confirms that the inversion resulted in the correct identification of the object's location and its dimensions. The contrast between brine and Plexiglas object (which is an isolating material) are inverted to be weaker than the actual contrast, due to smoothness-constraint type of inversion. However, the object is well defined and the discrepancy in the background area (brine) is kept to an acceptable minimum level. Moreover, for a porous material subjected to suffusion erosion processes resolving sharp contrasts between resistivity zones is not of primary interest. This is because the erosion patterns are produced smoothly by water flow. From this test it was concluded that the acquisition system was working correctly and the inversion model and boundaries were defined with enough accuracy.

3.2. 3D-ERT inversion and results

ERT data acquisitions were taken at the initial state of the specimen after material compaction and saturation and then repeated at predefined time intervals until the test was terminated. A total of 18 time-lapse measurements were taken during experiment A which had a duration of about 21 h, while 26 measurements were taken during experiment B, which lasted about 28 h. We inverted each dataset independently, without adopting any time-lapse inversion scheme, due to the fact that the changes of resistivity with time were well correlated and smooth. The same inversion parameters (i.e., the initial resistivity distribution guess, the fixed resistivity zones, and error estimation and weighting) were kept fixed for all the inversions belonging to each experiment. The errors associated to each measurement were used to fit the linear model suggested by Slater et al. (2000), whose parameters were provided as input to the inversion software.

After having performed the inversions, we calculated the 3D resistivity change from the initial state as follows:

$$\Delta\rho = \rho_0 - \rho_t \tag{9}$$

where ρ_0 (Ωm) refers to the initial resistivity distribution, and ρ_t (Ωm) the resistivity distribution at time *t* (hours), where a positive value of Δρ (Ωm) indicates a decrease in resistivity with respect to the initial distribution. A decrease in resistivity is considered to be directly correlated to a decrease of porosity.

The contours of resistivity changes for suffusion experiment A are presented in Fig. 9, at selected time intervals. For improving the visualization of the areas where the erosion took place (i.e., where a decrease in resistivity was observed), only the areas where $\Delta\rho > 0$ were retained in the figure.

In Fig. 9 the contours show that the resistivity change of the specimen started and developed mainly in the vicinity of one of the walls whereby during the course of experiment the process continued and in addition it has been observed in different locations. These resistivity changing spots grew in size of influence and as well as in deference with respect to the original resistivity magnitude. In fact, after the suffusion process is initiated, the soil matrix started to change due to the transport of the fine particles that increased the porosity. From the photographic evidence it can be observed that the test specimen's upper surface and the colour shade changed due to the eroded material; the grey areas in the picture are those where the finer material is not removed by erosion, while the reddish areas indicate the emergence of the coarse sandy gravel matrix where the finer part is removed. It is also notable that the final tomography image (t = 19 h) coherently overlaps with the picture of the top of the specimen, showing a similar pattern of change of the material being eroded mostly at the walls and less in the middle of the specimen.

Fig. 10 shows the resistivity changes at selected time instants for suffusion experiment B. Patterns similar to those for experiment A were found, showing that erosion processes triggered predominantly from areas close to the lateral walls of the erosion chamber. However, due to the vertical applied load of 10 kPa in this experiment, the distribution of the stresses inside the specimen was modified, having an impact on the initiation of internal erosion and on its trend with time.

As observed by Ferdos et al. (2018), the boundary effects due to the erosion chamber walls caused a non-linear stress distributions with depth, predominantly close to the walls due both to wall displacement and friction between the grains and the wall. These non-linear effects may justify the tendency of the processes to initiate in proximity of the sidewalls. As the process continued the fine particles were transported out from the specimen and a redistribution of the stresses in the solid compartment of the soil matrix occurred continuously with time. This process continued until it reached a critical limit where the forces induced by the fluid flow are no more capable of displacing the particles and the erosion rate decreased to almost zero.

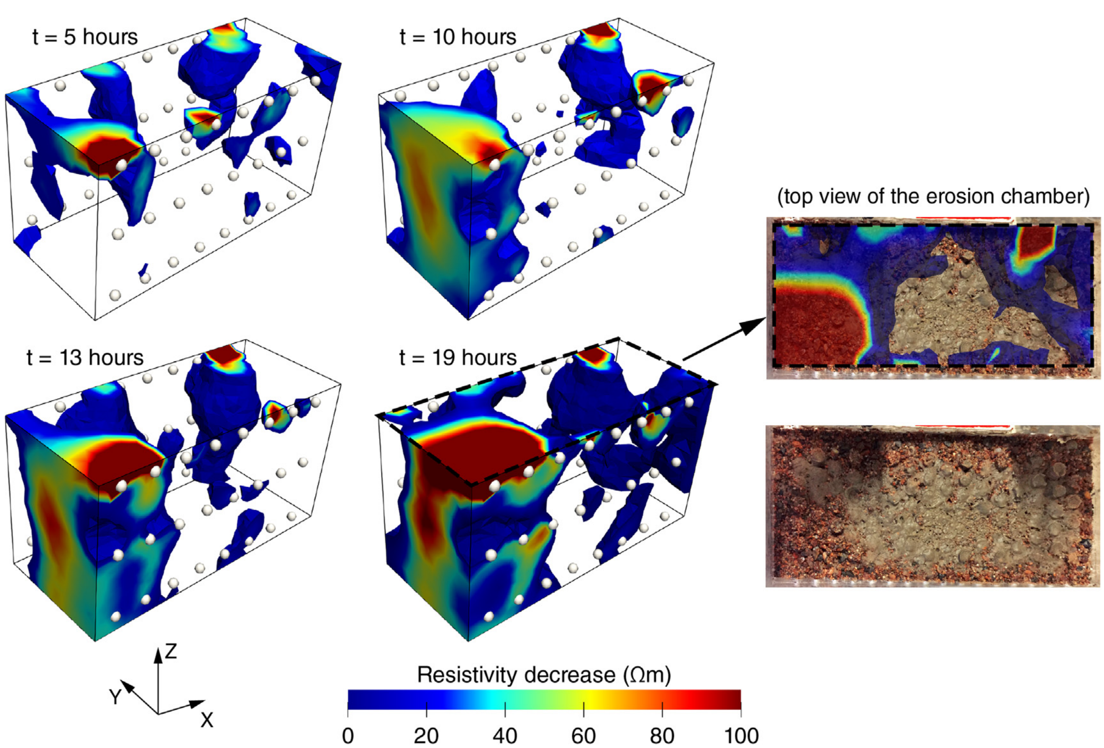

Fig. 9. Suffusion experiment A. Resistivity decrease from the initial resistivity after 5, 10, 13, and 19 h after erosion started and comparison of the last image with photographic evidence of eroded material.

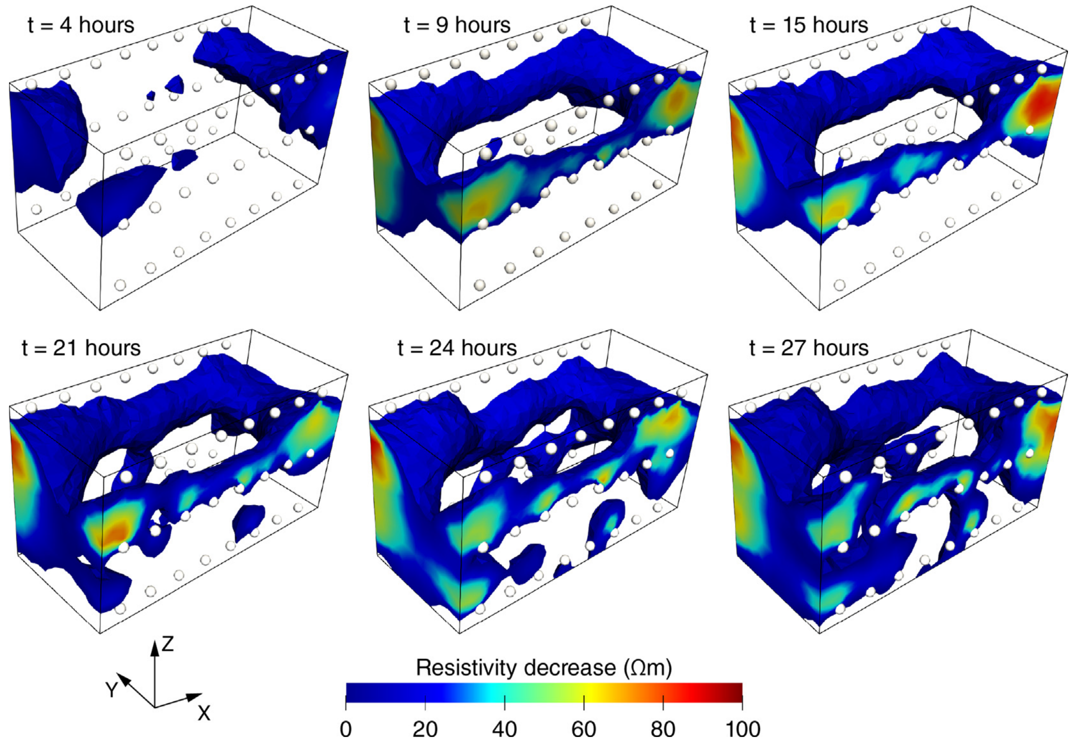

Fig. 10. Suffusion experiment B. Resistivity decrease from the initial resistivity after 4, 9, 15, 21, 24 and 27 h after erosion started.

3.3. Quantitative evaluation of the ERT measurements

Resistivity changes of a specimen in time, undergoing an internal erosion process, can be successively related to structural changes in the soil mix. That is if the tests are conducted under laboratory-controlled conditions where the only parameter that causes the resistivity changes in the sample is the structural changes. For this purpose, we used Eq. (8) to assess the changes in soil porosity from changes in resistivity.

In the application of Eq. (8) to the experiments carried out in the present study, we made the assumption that the magnitude of the surface conductivity is significantly smaller than the magnitude of water conductivity, thus the surface conductivity term can be neglected. This assumption is supported by the fact that the material used in the experiment was mainly composed of particles having a diameter larger than 0.06 mm as shown in Fig. 5, therefore no clay content was present in the soil mixture. The finer fraction of the soil was composed of silty-sandy particles and the coarser fraction of sand and gravel. For other particle size distributions having comparable diameter ranges, the contribution of the surface conductivity has been shown to be negligible by other authors (Bolève et al., 2011).

In applying Eq. (8), we also assumed 100% water saturation ($S_w = 1$), which remained constant during the experiments. This assumption holds also in the first phases of the experiment, as the saturation of the material was rapidly obtained after the application of the hydraulic head.

The following scheme is proposed to be used that relates the resistivity changes to erosion process evolution in the material. First, for each mesh cell of the model, the resistivity values are then transformed into porosity variations by adopting Eq. (10):

$$\Delta\phi = \phi(\rho_t) - \phi(\rho_0) \tag{10}$$

in which $\Delta\phi$ (–) is the porosity of the mesh cell at time t with respect to the initial state (t = 0). The total material that is lost due to the erosion processes for each mesh cell is related to the porosity change of the specimen. Therefore, the total eroded volume of material can be calculated from the 3D porosity variation ($\Delta\phi$) distribution:

$$V_e = \int_V \Delta\phi \; dV = \Delta\phi_{\text{mean}} \cdot V_{tot} \tag{11}$$

in which V_{tot} (m^3) is the total volume of the domain (i.e., the soil volume), dV (m^3) is the volume of each mesh cell, V_e (m^3) is the eroded volume, and $\Delta\phi_{mean}$ (-) is the volume-averaged porosity variation. The eroded material volume is also equal to the variation of the pore-space void volume V_v (m^3) by:

$$V_e = \Delta\phi_{\text{mean}} \cdot V_{tot} = \frac{\Delta V_v}{V_{tot}} V_{tot} = \Delta V_v \tag{12}$$

When the eroded volume is integrated from all the mesh cells, this volume can then be correlated to the eroded soil mass if the average specific weight (G_s) of the soil grains is known and is done by:

$$M = G_s \Delta V_v \tag{13}$$

in which M (kg) is the eroded mass and G_s (kg/m^3) was taken as 2537 kg/m^3 from Ferdos et al. (2018) for the soil mix used in their erosion studies. The eroded mass calculated from Eq. (13) is the cumulative eroded mass from the tests start to the time of the acquisition and its inversion.

To calibrate the Archie's law parameters, we used the inverted resistivities and the time-dependent mass removal data. A calibration loop of data fitting for Archie's law parameters was produced for each inversion and the resistivity changes were then converted into porosity change in media and finally translated to weight loss by Eq. (13). The weight loss at that specific time were compared with the cumulative eroded mass measured from the experiments. The Archie's law parameters were tuned to reach minimum error between the calculated eroded mass from ERT analysis and the collected data from the laboratory experiments.

This calibration process is schematically presented in Fig. 11.

We used the first dataset (suffusion experiment A) to perform the calibration with the proposed scheme, and the dataset of suffusion experiment B to validate the optimized model parameters. The optimization was carried out in MATLAB environment using a constrained version of the Nelder-Mead simplex algorithm.

The results of the calibration and validation of the Archie's law

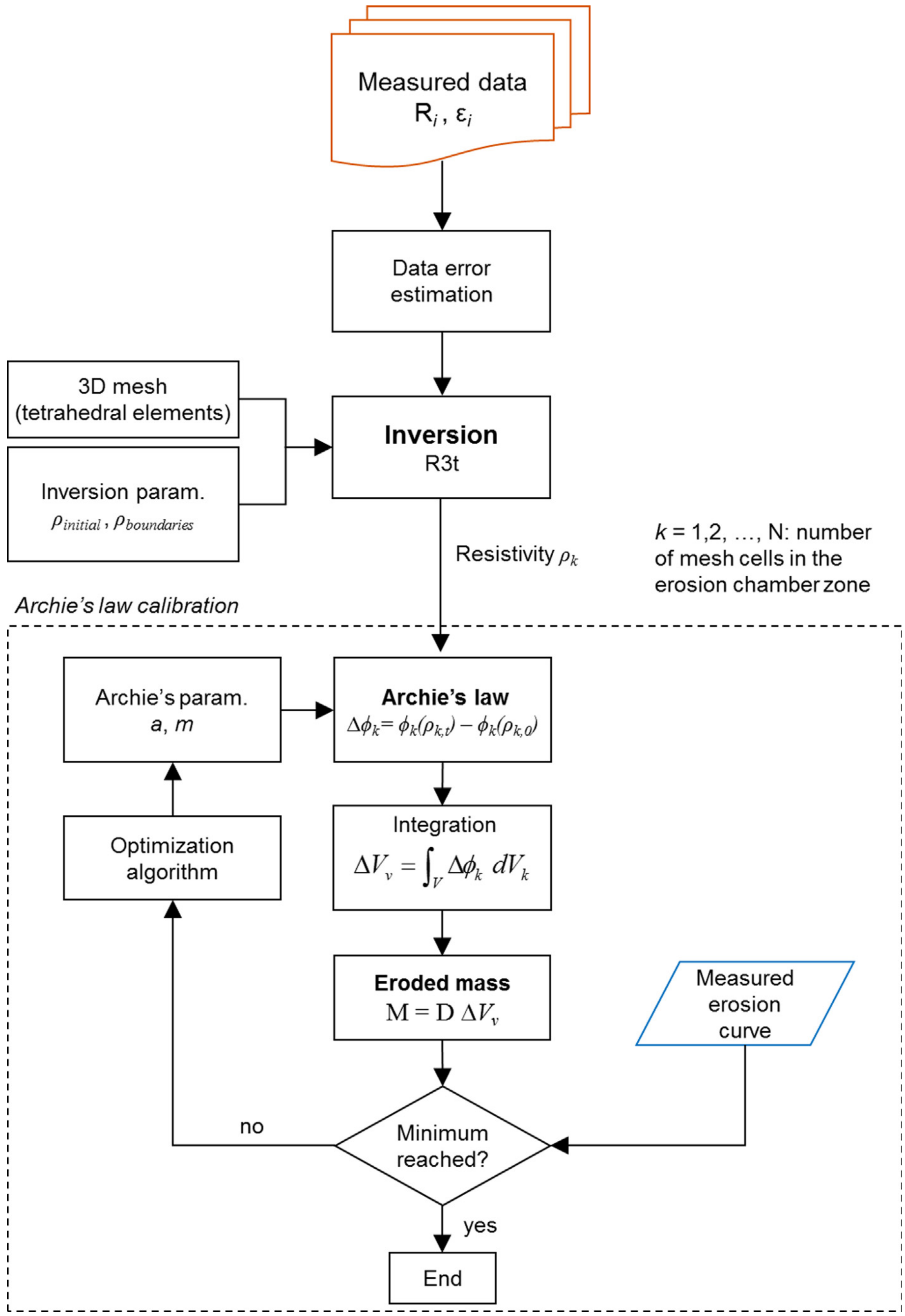

Fig. 11. Procedure for calibration of Archie's law parameters.

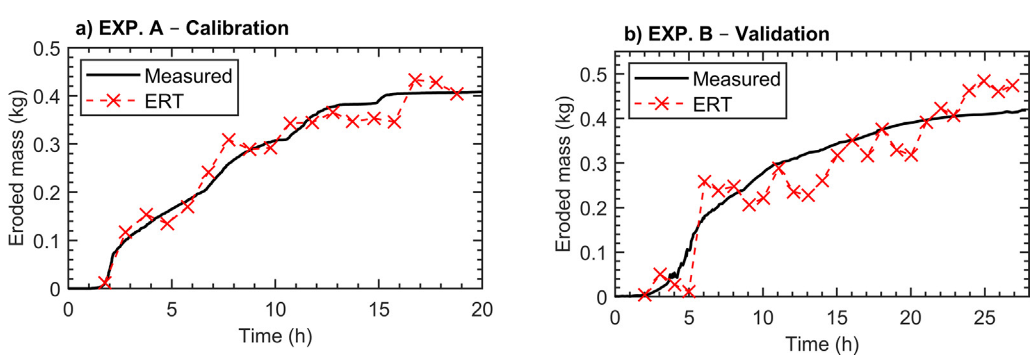

Fig. 12. Comparison between the measured eroded mass due to suffusion and the mass estimated from ERT data. a) Calibration dataset (suffusion experiment A); b) validation dataset (suffusion experiment B).

Table 2
Summary of the parameters and results from the calibration of Archie's law.

	EXP A – Calibration	EXP B – Validation	Unit
Measured water conductivity (start)	0.42	0.45	mS/cm
Measured water conductivity (end)	0.42	0.42	mS/cm
ERT initial resistivity (average)	304	245	Ωm
ERT final resistivity (average)	288	234	Ωm
Archie's – *a*	1.76	1.76	–
Archie's – *m*	1.42	1.42	–
Measured initial porosity	0.285	0.280	–
ERT estimated initial porosity	0.283	0.280	–
ERT estimated final porosity	0.298	0.299	–
Measured final eroded mass (average)	0.407	0.413	kg
ERT estimated final eroded mass	0.404	0.474	kg
RMSE. ERT vs measured	0.027	0.052	kg
R^2. ERT vs measured	0.95	0.87	–

parameters are presented in Fig. 12 and Table 2. In both calibration and validation, we used the measured water conductivity as input to the Archie's law; the ranges of water conductivity are reported in Table 2.

Fig. 12 illustrates the comparison between the measured and ERT-derived time-dependent cumulative of the eroded (dry) mass during the course of the experiments. As it can be seen from the results, in both experiments the removal rate (i.e., the time-derivative of the cumulative curve) was larger at the beginning of the experiment and gradually decreased with time. The erosion continued for about 20–25 h after reaching a minimum rate under the constant water head applied, after which the erosion process stopped.

The calibration yielded a value of 1.42 for the cementation exponent (m), which is very close to the values that are available in literature for unconsolidated material (e.g., $m \approx 1.3$ for unconsolidated sands). The parameter a slightly exceeded the expected range ($a \approx 1$) indicating that a source of systematic error may be present in the adopted measurement or inversion scheme. This is likely to be related to the inversion process, in which the error weights could be overestimated or underestimated due to the lack of reciprocal measurements, leading to systematic errors in the resolution of the resistivity distributions. However, as confirmed by the model validation (RMSE = 0.052 kg, R^2 = 0.87), the results are successfully reproducible. In the estimated eroded mass curves, as shown in Fig. 12, the overall mass balances are preserved, even if the fluctuation of the ERT-derived points can be observed. This may represent a drawback when trying to estimate the global erosion rate, i.e., by taking the time-derivative of the cumulate curves. The quantification of the instantaneous rate with this method might be rather inaccurate; a possible solution is to estimate the overall erosion rate by time-averaging multiple points of the ERT curves, however, this operation would decrease the time resolution of the method for fast erosion processes. On the contrary, when the time-scale of the erosion processes is much slower than the measurement periods, the time-averaging technique would lead to a more accurate estimation of the erosion rates.

Under the specific experimental conditions, the resistivity variations captured by ERT imaging are related to relatively small changes in the porosity values, therefore in this particular case it is crucial to acquire the data with a high-resolution technique and tightly spaced electrodes. In fact, the sensitivity of the calibrated Archie's model parameters to the resistivity input may, in some cases, exceed the sensitivity and resolution of the ERT images, especially in the zones located far away from the electrode arrays. The reduced sensitivity may induce an underestimation of the erosion rates or can bias the results of the model calibration procedures. From Fig. 10, this can be observed in the middle of the specimen, where the combination of both reduced sensitivity and lower erosion magnitude lead to the presence of a central zone where resistivity changes are below an observable threshold. However, the influence of this issue to the overall result may be limited in this study, as the validation errors (RMSE, R^2 in Table 2) are still within an acceptable level.

The reduction is sensitivity however, may pose a critical limitation in the field application of this technique, mainly because of the practical obstacles which necessarily cause a reduced sensitivity of ERT in the field. To name a few: the difficulty of installing 3D arrays, the limited number of installable electrodes, the number of available ADC channels of the measurement equipment, the higher background electromagnetic noise (compared to the laboratory), the increased electrode contact impedance, the large amount of data to be collected, stored and processed, and the overall costs related to the implementation of high-resolution surveys. In conclusion, the success of an ERT investigation in the field strictly depends on both the spatial and time-scale at which the phenomena occur in combination with the adopted measurement and processing strategies.

4. Conclusions

We used electrical resistivity tomography (ERT) technique to monitor internal erosion in porous media induced by seepage flow; this phenomenon is one of the most common causes of failure of earthen levees and embankment dams. An ERT system was specifically designed for the time-lapse imaging of the electrical properties of porous media at a laboratory scale. The components of the systems were optimized to specific requirements in terms of accuracy and speed of acquisition, due to the time-dependent nature of erosion processes. The electrode material and positioning were investigated, the latter by numerical modelling which allowed us to define the proper electrode installation requirements for the minimization of the errors due to electrode polarization. The system operated with a total of 48 electrodes, with multi-channel voltage readings of up to 6 electrodes simultaneously. We validated the forward and inverse models by seeking for optimal choice of the boundary conditions, studying the numerical model sensitivity to mesh size, and by experimentally testing the measurement and inversion setup with a known resistivity distribution.

Two erosion (i.e., suffusion) tests were performed to reproduce the process of internal erosion of soil particles by water flow within a purposely prepared soil mixture, under two different mechanical loadings (0 and 10 kPa vertical stress application on the top of the specimen). 3D time-lapse monitoring of internal erosion was carried out, at regular intervals of 1 h.

To relate resistivity variations to material structural changes in time during the erosion processes we calculated the porosity variations through the Archie's law, with parameters calibrated using both the results from the inversions and the measured cumulate of the material eroded from the test chamber. Comparison of the 3D tomography results with the mass removal data as well as the validation of the identifies Archie's parameters were found to be successful.

We can conclude that ERT technique is potentially capable of detecting and quantifying the erosion processes in dams and levees. The practical aspects when conducting an ERT survey in the field, compared to the controlled conditions in the laboratory, may represent a limiting factor to the use this technique in real world applications, especially with regards to the electrode installation and the limits in installing high-resolution 3D arrays in the field. However, we successfully demonstrated that the method is robust and reliable, provided that extensive supplementary information is necessary, which should be integrated with the ERT survey data.

CRediT authorship contribution statement

Matteo Masi: Conceptualization, Methodology, Software, Validation, Data curation, Writing - original draft, Visualization.

Farzad Ferdos: Conceptualization, Methodology, Investigation, Data curation, Writing - original draft, Visualization, Project administration. **Gabriella Losito:** Conceptualization, Formal analysis, Writing - review & editing. **Luca Solari:** Conceptualization, Writing - review & editing, Supervision, Project administration.

Declaration of Competing Interest

The authors declare that they have no known competing financial interests or personal relationships that could have appeared to influence the work reported in this paper.

Acknowledgements

This study was performed as part of a joint research project in-between the Royal Institute of Technology (KTH, Sweden) and Department of Civil and Environmental Engineering (DICEA) of the University of Florence (Italy) and was funded by the Swedish Hydropower Centre (Svenskt Vattenkraft Centrum, SVC), with funding project number VK10739. The authors acknowledge Vattenfall for the help and support in conducting the experiments at Vattenfall R&D laboratory in Älvkarleby, Sweden. The authors are thankful to two anonymous reviewers, whose comments and suggestions helped us to improve the quality of the manuscript.

References

Al-Fares, W., 2011. Contribution of the geophysical methods in characterizing the water leakage in Afamia B dam, Syria. J. Appl. Geophys. 75, 464–471. https://doi.org/10.1016/J.JAPPGEO.2011.07.014.

Al-Fares, W., 2014. Application of electrical resistivity tomography technique for characterizing leakage problem in Abu Baara Earth Dam, Syria. Int. J. Geophys. 2014, 368128. https://doi.org/10.1155/2014/368128.

Alnæs, M.S., Blechta, J., Hake, J., Johansson, A., Kehlet, B., Logg, A., Richardson, C., Ring, J., Rognes, M.E., Wells, G.N., 2015. The FEniCS Project Version 1.5. Arch. Numer. Softw. 3.

Archie, G.E., 1942. The electrical resistivity log as an aid in determining some reservoir characteristics. Pet. Technol. 54–62. https://doi.org/10.2118/942054-G.

Bakker, M.A.J., Van Der Meer, J.J.M., 2003. Structure of a Pleistocene push moraine revealed by GPR: the eastern Veluwe Ridge, The Netherlands. Geol. Soc., London, Spec. Publ. 211 (1), 143–151. https://doi.org/10.1144/GSL.SP.2001.211.01.12.

Binley, A., 2015. Tools and techniques: electrical methods. Treatise Geophys. 233–259. https://doi.org/10.1016/B978-0-444-53802-4.00192-5.

Binley, A., 2019. R3t version 2.0 User Guide [WWW Document]. Lancaster Univ.

Binley, A., Kemna, A., 2005. DC resistivity and induced polarization methods. In: Rubin, Y., Hubbard, S. (Eds.), Hydrogeophysics SE - 5. Water Science and Technology Library. Springer, Netherlands, pp. 129–156. https://doi.org/10.1007/1-4020-3102-5_5.

Bolève, A., Janod, F., Revil, A., Lafon, A., Fry, J.-J., 2011. Localization and quantification of leakages in dams using time-lapse self-potential measurements associated with salt tracer injection. J. Hydrol. 403, 242–252. https://doi.org/10.1016/J.JHYDROL.2011.04.008.

Bonelli, S., Nicot, F., 2013. Erosion in Geomechanics Applied to Dams and Levees. https://doi.org/10.1002/9781118577165.

Breede, K., Kemna, A., Esser, O., Zimmermann, E., Vereecken, H., Huisman, J.A., 2011. Joint measurement setup for determining spectral induced polarization and soil hydraulic properties. Vadose Zo. J. https://doi.org/10.2136/vzj2010.0110.

Carlsten, S., Johansson, S., Wörman, A., 1995. Radar techniques for indicating internal erosion in embankment dams. J. Appl. Geophys. 33, 143–156. https://doi.org/10.1016/0926-9851(95)90037-3.

Chambers, J., Ogilvy, R., Kuras, O., Cripps, J., Meldrum, P., 2002. 3D electrical imaging of known targets at a controlled environmental test site. Environ. Geol. 41, 690–704. https://doi.org/10.1007/s00254-001-0452-4.

Chambers, J.E., Wilkinson, P.B., Kuras, O., Ford, J.R., Gunn, D.A., Meldrum, P.I., Pennington, C.V.L., Weller, A.L., Hobbs, P.R.N., Ogilvy, R.D., 2011. Three-dimensional geophysical anatomy of an active landslide in Lias Group mudrocks, Cleveland Basin, UK. Geomorphology 125, 472–484. https://doi.org/10.1016/J.GEOMORPH.2010.09.017.

Cho, I.-K., Yeom, J.-Y., 2007. Crossline resistivity tomography for the delineation of anomalous seepage pathways in an embankment dam. Geophysics 72, G31–G38. https://doi.org/10.1190/1.2435200.

Constable, S.C., Parker, R.L., Constable, C.G., 1987. Occam's inversion: a practical algorithm for generating smooth models from electromagnetic sounding data. Geophysics 52, 289–300.

Dahlin, T., Johansson, S., 1995. Resistivity variations in an earth embankment dam in Sweden. In: 1st EEGS Meeting. European Association of Geoscientists & Engineers, https://doi.org/10.3997/2214-4609.201407463. p. cp-63-00078.

Dahlin, T., Sjödahl, P., Friborg, J., Johansson, S., 2001. Resistivity and SP surveying and monitoring at the Sädva Embankment Dam, Sweden. In: Mistømme, G.H., Honningsvåg, B., Repp, K., Vaskinn, K.A., Westeren, T. (Eds.), Procs. 5th European ICOLD Symposium, pp. 107–113.

Dahlin, T., Bernstone, C., Loke, M.H., 2002. A 3-D resistivity investigation of a contaminated site at Lernacken, Sweden. Geophysics 67, 1692–1700. https://doi.org/10.1190/1.1527070.

Daily, W., Owen, E., 1991. Cross-borehole resistivity tomography. Geophysics 56, 1228–1235. https://doi.org/10.1190/1.1443142.

De Donno, G., Cardarelli, E., 2011. Assessment of errors from different electrode materials and configurations for electrical resistivity and time-domain IP data on laboratory models. Boll. di Geofis. Teor. ed Appl. 52, 211–223.

Deceuster, J., Kaufmann, O., Van Camp, M., 2013. Automated identification of changes in electrode contact properties for long-term permanent ERT monitoring experiments. Geophysics 78, E79–E94. https://doi.org/10.1190/geo2012-0088.1.

deGroot-Hedlin, C., Constable, S., 1990. Occam's inversion to generate smooth, two-dimensional models from magnetotelluric data. Geophysics 55, 1613–1624.

Fargier, Y., Lopes, S.P., Fauchard, C., François, D., Côte, P., 2014. DC-Electrical Resistivity Imaging for embankment dike investigation: a 3D extended normalisation approach. J. Appl. Geophys. 103, 245–256. https://doi.org/10.1016/J.JAPPGEO.2014.02.007.

Fell, R., Wan, C.F., Cyganiewicz, J., Foster, M., 2003. Time for development of internal erosion and piping in embankment dams. J. Geotech. Geoenvironmental Eng. 129, 307–314. https://doi.org/10.1061/(ASCE)1090-0241(2003)129:4(307).

Ferdos, F., Dargahi, B., Solari, L., 2018. Mechanism of suffusion erosion phenomenon in porous media. J. Geol. Geosci. 2 (1).

Geuzaine, C., Remacle, J.-F., 2009. Gmsh: a 3-D finite element mesh generator with built-in pre- and post-processing facilities. Int. J. Numer. Meth. Eng. 79, 1309–1331. https://doi.org/10.1002/nme.2579.

Gharibi, M., Bentley, L.R., 2005. Resolution of 3-D electrical resistivity images from inversions of 2-d orthogonal lines. J. Environ. Eng. Geophysics 10, 339–349. https://doi.org/10.2113/JEEG10.4.339.

Glover, P.W.J., 2016. Archie's law – a reappraisal. Solid Earth 7, 1157–1169. https://doi.org/10.5194/se-7-1157-2016.

Hirsch, M., Bentley, L.R., Dietrich, P., 2008. A Comparison of electrical resistivity, ground penetrating radar and seismic refraction results at a river terrace site. J. Environ. Eng. Geophys. 13, 325–333. https://doi.org/10.2113/JEEG13.4.325.

Ikard, S.J., Revil, A., Jardani, A., Woodruff, W.F., Parekh, M., Mooney, M., 2012. Saline pulse test monitoring with the self-potential method to nonintrusively determine the velocity of the pore water in leaking areas of earth dams and embankments. Water Resour. Res. 48. https://doi.org/10.1029/2010WR010247.

Ikard, S.J., Rittgers, J., Revil, A., Mooney, M.A., 2015. Geophysical investigation of seepage beneath an Earthen Dam. Groundwater 53, 238–250. https://doi.org/10.1111/gwat.12185.

Johansson, S., Dahlin, T., 1996. Seepage monitoring in an earth embankment dam by repeated resistivity measurements. Euro. J. Eng. Environ. Geophys. 1, 229–247.

Kemna, A., 2000. Complex resistivity tomography for environmental applications. Chem. Eng. J. 77, 11–18. https://doi.org/10.1016/S1385-8947(99)00135-7.

LaBrecque, D., Daily, W., 2008. Assessment of measurement errors for galvanic-resistivity electrodes of different composition. Geophysics 73, F55–F64. https://doi.org/10.1190/1.2823457.

Lesur, V., Cuer, M., Straub, A., 1999a. 2-D and 3-D interpretation of electrical tomography measurements, Part 1: the forward problem. Geophysics 64, 386–395. https://doi.org/10.1190/1.1444543.

Lesur, V., Cuer, M., Straub, A., 1999b. 2-D and 3-D interpretation of electrical tomography measurements, Part 2: the inverse problem. Geophysics 64, 396–402. https://doi.org/10.1190/1.1444544.

Loke, M.H., Barker, R.D., 1995. Least-squares deconvolution of apparent resistivity pseudosections. Geophysics 60, 1682–1690.

Loke, M.H., Wilkinson, P.B., Uhlemann, S.S., Chambers, J.E., Oxby, L.S., 2014. Computation of optimized arrays for 3-D electrical imaging surveys. Geophys. J. Int. 199, 1751–1764. https://doi.org/10.1093/gji/ggu357.

Masi, M., Losito, G., 2015. Spectral induced polarization for monitoring electrokinetic remediation processes. J. Appl. Geophys. 123, 284–294. https://doi.org/10.1016/j.jappgeo.2015.08.011.

Moore, J.R., Boleve, A., Sanders, J.W., Glaser, S.D., 2011. Self-potential investigation of moraine dam seepage. J. Appl. Geophys. 74, 277–286. https://doi.org/10.1016/J.JAPPGEO.2011.06.014.

Panthulu, T.V., Krishnaiah, C., Shirke, J.M., 2001. Detection of seepage paths in earth dams using self-potential and electrical resistivity methods. Eng. Geol. 59, 281–295. https://doi.org/10.1016/S0013-7952(00)00082-X.

Park, S.K., Van, G.P., 1991. Inversion of pole-pole data for 3-D resistivity structure beneath arrays of electrodes. Geophysics 56, 951–960. https://doi.org/10.1190/1.1443128.

Rittgers, J.B., Revil, A., Planes, T., Mooney, M.A., Koelewijn, A.R., 2014. 4-D imaging of seepage in earthen embankments with time-lapse inversion of self-potential data constrained by acoustic emissions localization. Geophys. J. Int. 200, 758–772. https://doi.org/10.1093/gji/ggu432.

Schmutz, M., Revil, A., Vaudelet, P., Batzle, M., Viñao, P.F., Werkema, D.D., 2010. Influence of oil saturation upon spectral induced polarization of oil-bearing sands. Geophys. J. Int. 183, 211–224. https://doi.org/10.1111/j.1365-246X.2010.04751.x.

Schön, J.H., 2015. Physical Properties of Rocks: Fundamentals and Principles of Petrophysics. Elsevier.

Shima, H., 1992. 2-D and 3-D resistivity image reconstruction using crosshole data. Geophysics 57, 1270–1281. https://doi.org/10.1190/1.1443195.

Shin, S., Park, S., Kim, J.-H., 2019. Time-lapse electrical resistivity tomography characterization for piping detection in earthen dam model of a sandbox. J. Appl.

Geophys. 170, 103834. https://doi.org/10.1016/J.JAPPGEO.2019.103834.
Sjödahl, P., Dahlin, T., Johansson, S., 2005. Using resistivity measurements for dam safety evaluation at Enemossen tailings dam in southern Sweden. Environ. Geol. 49, 267–273. https://doi.org/10.1007/s00254-005-0084-1.
Sjödahl, P., Dahlin, T., Johansson, S., Loke, M.H., 2008. Resistivity monitoring for leakage and internal erosion detection at Hällby embankment dam. J. Appl. Geophys. 65, 155–164. https://doi.org/10.1016/J.JAPPGEO.2008.07.003.
Sjödahl, P., Dahlin, T., Johansson, S., 2010. Using the resistivity method for leakage detection in a blind test at the Røssvatn embankment dam test facility in Norway. Bull. Eng. Geol. Environ. 69, 643–658. https://doi.org/10.1007/s10064-010-0314-y.
Skempton, A.W., Brogan, J.M., 1994. Experiments on piping in sandy gravels. Géotechnique 44, 449–460. https://doi.org/10.1680/geot.1994.44.3.449.
Slater, L., Binley, A., Daily, W., Johnson, R., 2000. Cross-hole electrical imaging of a controlled saline tracer injection. J. Appl. Geophys. 44, 85–102. https://doi.org/10.1016/S0926-9851(00)00002-1.
Smith, D.G., Jol, H.M., 1992. Ground-penetrating radar investigation of a Lake Bonneville deita, Provo level, Brigham City, Utah. Geology 20, 1083–1086. https://doi.org/10.1130/0091-7613(1992)020 < 1083:GPRIOA > 2.3.CO;2.
Soueid Ahmed, A., Revil, A., Bolève, A., Steck, B., Vergniault, C., Courivaud, J.R., Jougnot, D., Abbas, M., 2020. Determination of the permeability of seepage flow paths in dams from self-potential measurements. Eng. Geol. 268, 105514. https://doi.org/10.1016/J.ENGGEO.2020.105514.
Titov, K., Loukhmanov, V., Potapov, A., 2000. Monitoring of water seepage from a reservoir using resistivity and self polarization methods: case history of the Petergoph fountain water supply system. First Break 18, 431–435. https://doi.org/10.1046/j.1365-2397.2000.00096.x.
Trafford, A., 2009. Mapping thickness of raised peat bog deposits using GPR. In: Near Surface 2009 – 15th European Meeting of Environmental and Engineering Geophysics, https://doi.org/10.3997/2214-4609.20147058.
Vanhala, H., Soininen, H., 1995. Laboratory technique for measurement of spectral induced polarization response of soil sampies. Geophys. Prospect. 43, 655–676.
Wan, C.F., Fell, R., 2008. Assessing the potential of internal instability and suffusion in embankment dams and their foundations. J. Geotech. Geoenviron. Eng. https://doi.org/10.1061/(ASCE)1090-0241(2008)134:3(401).
Waxman, M.H., Smits, L.J.M., 1968. Electrical conductivities in oil-bearing Shaly Sands. Soc. Pet. Eng. J. 8, 107–122. https://doi.org/10.2118/1863-A.
Zimmermann, E., Kemna, A., Berwix, J., Glaas, W., Vereecken, H., 2008. EIT measurement system with high phase accuracy for the imaging of spectral induced polarization properties of soils and sediments. Meas. Sci. Technol. 19, 94010.